

## Negative Poisson's ratio in puckered two-dimensional materials

Bei Liu,<sup>1</sup> Mengqi Niu,<sup>1,2</sup> Jia Fu,<sup>1,2</sup> Zeyu Xi,<sup>1</sup> Ming Lei,<sup>1,\*</sup> and Ruge Quhe<sup>1,\*</sup>

<sup>1</sup>State Key Laboratory of Information Photonics and Optical Communications and School of Science, Beijing University of Posts and Telecommunications, Beijing 100876, People's Republic of China

<sup>2</sup>School of Electronic Engineering, Beijing University of Posts and Telecommunications, Beijing 100876, China



(Received 27 January 2019; revised manuscript received 10 April 2019; published 21 May 2019)

The experimentally verified negative Poisson's ratio of black phosphorus allows the extension of the medical and defense applications to the nanoscale regime without any artificial engineering. With a structure analogous to monolayer black phosphorus, monolayer SiS, SiSe, SnTe, and W-phase antimonene are predicted to show auxetic behavior, while a W-phase antimonene does not by using first-principles calculations. By putting these systems into a collective perspective with other puckered two-dimensional (2D) materials, we further formulate a uniform mechanism that could explain the different types of out-of-plane Poisson's ratio in the puckered 2D materials including monolayer group V-enes (BP, As, and Sb) and group IV monochalcogenides (SiS, SiSe, GeS, GeSe, SnS, SnSe, and SnTe). We found that both the structure and composition of the puckered monolayers play important roles in the out-of-plane Poisson's ratio.

DOI: [10.1103/PhysRevMaterials.3.054002](https://doi.org/10.1103/PhysRevMaterials.3.054002)

### I. INTRODUCTION

Poisson's ratio is a fundamental mechanical property of materials, characterizing the resulting strain in the transverse direction under a longitudinal uniaxial load. In most cases, the Poisson's ratio of a material is positive, i.e., the material contracts laterally when stretched and expands laterally when compressed. However, some materials show a negative Poisson's ratio (NPR), termed as the auxetic effect [1]. The auxetic effect can lead to enhanced mechanical properties, such as shear modulus [2], indentation resistance [3], and fracture toughness [4]. As a result, the auxetic materials have been proposed for applications in the fields of biomedicine, sensors, and national security and defense [5–7].

For a long time, the studies of the auxetic effect have been focused on the macroscopic materials since Lakes reported the NPR in the designed re-entrant foam in 1987 [8]. The auxetic effect of this foam derived from the engineering of its microstructures [9]. In addition to microstructure engineering, the auxetic effect can also be derived from the intrinsic properties of bulk-scale materials, such as some cubic materials [10,11] (both FCC and BCC),  $\alpha$ -cristobalite (SiO<sub>2</sub>) [12], and  $\alpha$ -TeO<sub>2</sub> [13].

Recently, the problem of auxeticity of two-dimensional (2D) membranes has been actively discussed in the literature in the context of suspended graphene [14–20]. The emergence of auxeticity of graphene is connected with out-of-plane dynamical and static deformations and is qualitatively consistent with expectations based on the membrane theory [21]. Moreover, it is found that the Poisson's ratio can be tuned by stress [22,23]. 2D materials such as 2D silicon dioxide [24], pentagraphene [25,26], Be<sub>5</sub>C<sub>2</sub> [27],  $h\alpha$ -silica [28], and 1T-type transition metal dichalcogenides [29] were predicted

to show in-plane NPR. In monolayer black phosphorus with a puckered structure [30,31], out-of-plane NPR (−0.027) predicted by first-principles calculations has been verified experimentally [32,33]. Later, a series of 2D materials including 2D arsenic [34], GeS [35], and Ag<sub>2</sub>S [36] have been predicted to show out-of-plane NPR, and this NPR is considered to originate from the puckered crystal structures analog to black phosphorus. It is natural to ask whether the puckered structure in 2D materials guarantee a negative out-of-plane Poisson's ratio. It is worth noticing that the out-of-plane NPR appears along the armchair ( $x$ ) direction in some of these puckered 2D materials, while along the zigzag ( $y$ ) direction in other ones. A universal understanding of the Poisson's ratio that covers all the puckered 2D materials is highly desired.

In this study, we first use first-principles calculations to study the structural and mechanical properties of monolayer group-IV monochalcogenides SiS, SiSe, and SnTe and group V-enes orthorhombic antimonene. Monolayer SiS, SiSe, SnTe, and W-phase antimonene possess a negative out-of-plane Poisson's ratio, while monolayer  $\alpha$ -W-phase antimonene does not. With the change of the applied strain strength, a sign change of the Poisson's ratio is found in monolayer SiSe and SnTe, along with a structural phase transformation. With the collective consideration of all the puckered 2D materials, a universal deformation mechanism for the intrinsic Poisson's ratio of puckered structures (including monolayer BP, As, Sb, SiS, SiSe, GeS, GeSe, SnS, SnSe, and SnTe) is proposed.

### II. METHODS

All calculations are performed within the framework of density functional theory, using the projector augmented wave method [37] as implemented in Vienna Ab Initio Simulation Package (VASP) [38]. The exchange-correlation term has been described within the generalized gradient approximation parameterized by the Perdew-Burke-Ernzerhof (PBE) functional

\*Corresponding authors: quheruge@bupt.edu.cn; mlei@bupt.edu.cn

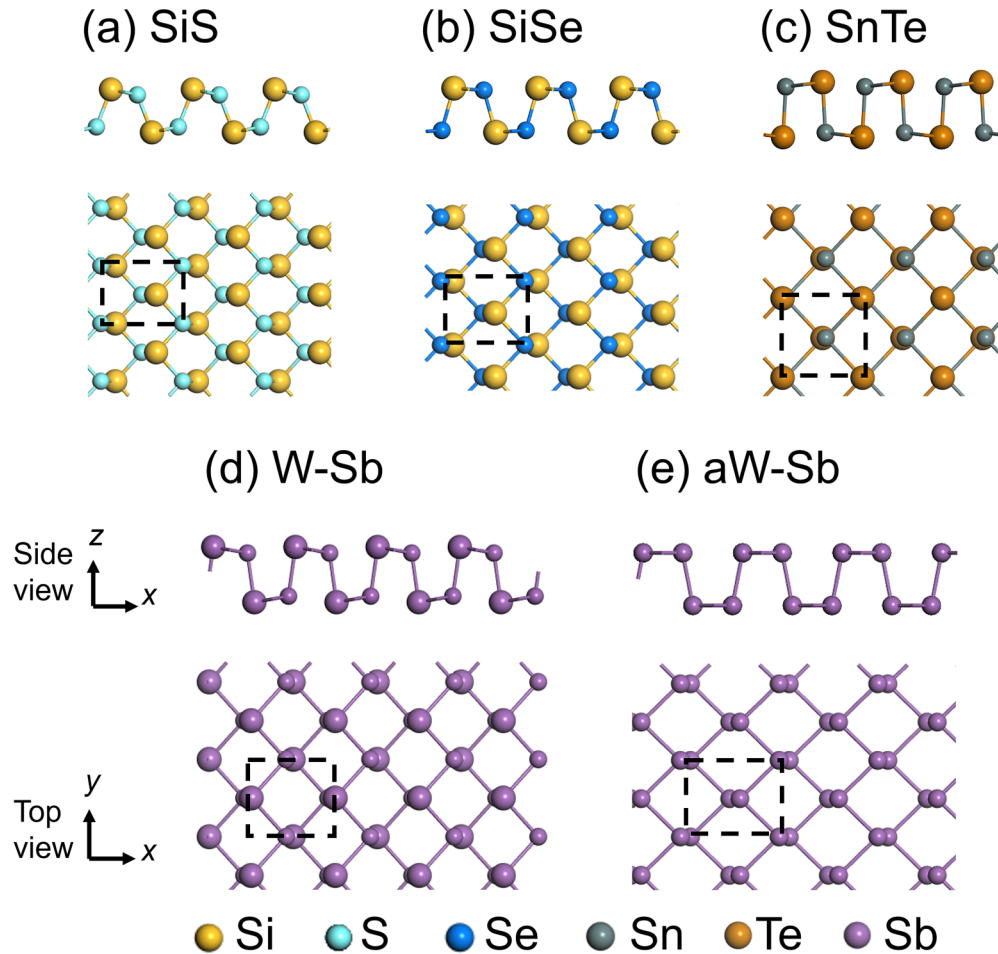


FIG. 1. Optimized structures of monolayer SiS (a), SiSe (b), SnTe (c), W-Sb (d), and aW-Sb (e). The out-most and inner atoms in the puckered layer are indicated by the balls with big and small size, respectively. Top image is the side view of optimized structures. Bottom image is top view of the optimized structures, showing a honeycomb-like structure. The armchair direction is the  $x$  direction and the pucker is along the  $y$  direction. The dashed area represents the primitive unit cell.

[39]. The kinetic energy cutoff is set to 420 eV for the plane wave expansion. All the structures are fully relaxed in the conjugant gradient method and the convergence threshold is set as  $10^{-4}$  eV for energy and 0.01 eV/Å for force. A  $6 \times 4 \times 1$  grid for  $k$ -point sampling is used for geometry optimization, while  $30 \times 22 \times 1$  is used for the free energy calculations.

The uniaxial strain in the  $x$  or  $y$  direction is applied by fixing the lattice constant in this direction to a value different from its strain-free value, e.g., the uniaxial compressible/tensile strain in a certain direction is realized by decreasing/increasing the lattice parameter in this direction. The corresponding strain is defined as  $\varepsilon = (L_i - L_0)/L_0$ , where  $L_i$  and  $L_0$  are the lattice constants under a certain strain and that of a strain-free system, respectively. Under the uniaxial strain, the atom positions and the lattice constants in the transverse directions are fully optimized.

### III. RESULTS AND DISCUSSION

#### A. Crystal structure

2D puckered SiS and SiSe are predicted to be energetically and dynamically stable [40–43], and might be isolated by mechanical, sonicated or liquid-phase exfoliation [44]. 2D

puckered SnTe has been fabricated by the molecular beam epitaxy technique [45,46]. It is noted that puckered SiS is a metastable structural phase [47], and the actual stable structure is the one with  $Pma2$  symmetry [48]. Monolayer SiS and SiSe are promising for electrode materials in lithium ion batteries [49] and photocatalysis [44]. Ferroic behavior of phosphorene and 2D group-IV monochalcogenides has been established by Mehboudi and coworkers [50]. Later, finite temperature behaviors in these materials such as structural transition [51,52], pyroelectricity [53], and anisotropic thermal expansion [54] have been deeply explored.

As shown in Figs. 1(a)–1(c), the optimized configurations of monolayer SiS and SiSe are similar to the puckered structure of monolayer black phosphorus, where the pucker can be regarded as a re-entrant structure that is comprised of two coupled orthogonal hinges [32]. The important geometrical parameters are listed in Table SI (Supplemental Material [55]). The armchair and zigzag directions are noted as the  $x$  and  $y$  directions, respectively. From the side view, SiS, SiSe, and SnTe show a Si-S-S-Si, Si-Se-Se-Si, and Te-Sn-Sn-Te four-layer puckered binary structure, respectively. This four-atomic-layer structure is different from the double-layer puckered structure of monolayer black phosphorus and arsenic [34].

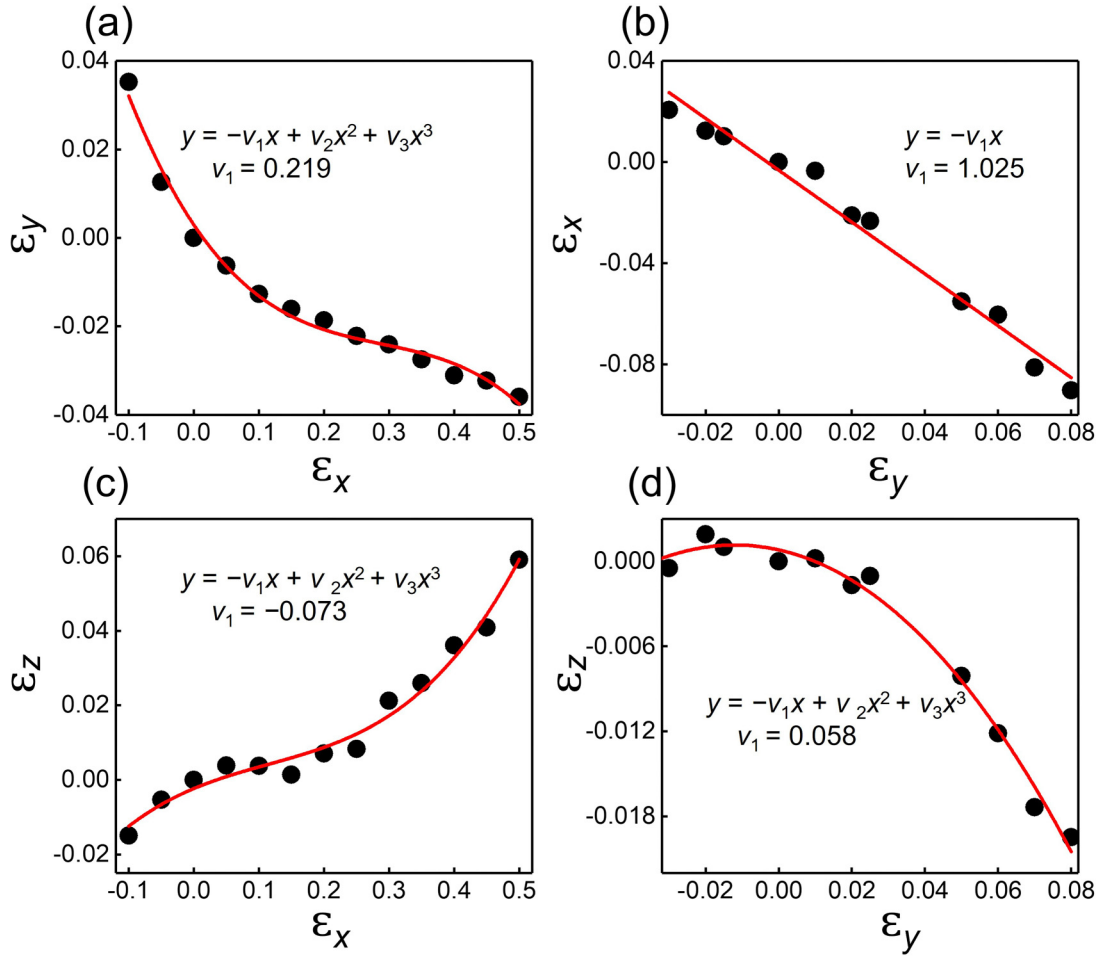


FIG. 2. Poisson's ratio as a function of uniaxial strain of monolayer SiS in the  $x$  direction (a), (c), and  $y$  direction (b), (d). (a)  $\varepsilon_y$  versus  $\varepsilon_x$ . Data are fitted to function  $y = -v_1x + v_2x^2 + v_3x^3$ , with  $v_1 = 0.219$  as the linear Poisson's ratio. (b)  $\varepsilon_x$  versus  $\varepsilon_y$ . Data are fitted to function  $y = -v_1x$ , with  $v_1 = 1.025$  as the linear Poisson's ratio. (c)  $\varepsilon_z$  versus  $\varepsilon_x$ . Data are fitted to function  $y = -v_1x + v_2x^2 + v_3x^3$ , with  $v_1 = -0.073$  as the linear Poisson's ratio. (d)  $\varepsilon_z$  versus  $\varepsilon_y$ . Data are fitted to function  $y = -v_1x + v_2x^2 + v_3x^3$ , with  $v_1 = 0.058$  as the linear Poisson's ratio.

From the top view, monolayer SiS and SiSe show a distorted honeycomb structure with two edges much shorter than the other four. We further studied the free energy of the three group-IV monochalcogenides as a function of different lattice parameters (see Fig. S1 in the Supplemental Material [55]).

Monolayer group V elementals antimonene has two puckered structural phases (W-Sb and aW-Sb) [Figs. 1(d)–1(f)]. These two phases are predicted to be dynamically stable [56,57]. Monolayer and bilayer antimonene with a puckered honeycomb structure have been fabricated on either  $\text{WTe}_2$  or bismuthene layers [58,59]. The W-phase antimonene shows a double-atomic-layer structure, while the aW-phase antimonene shows a four-atomic-layer structure. Their thickness are 2.79 and 3.19 Å, respectively. The calculated key structural parameters are in good agreement with previous theoretical works [57,60,61].

### B. Poisson's ratio

We investigated the in-plane and out-of-plane Poisson's ratio under the  $x$ -directional strain of  $-10$ – $50\%$  and the  $y$ -directional strain of  $-3$ – $8\%$ , respectively. For nearly linear behaviors, the data are fitted to the function  $y = -v_1x$ ,

where  $v_1$  is the linear Poisson's ratio. For strong nonlinear behaviors, the data are fitted to the function  $y = -v_1x + v_2x^2 + v_3x^3$ , where  $v_1$  can be regarded as the linear Poisson's ratio [32].

The Poisson's ratios of monolayer SiS for uniaxial strain in the  $x$  direction and in the  $y$  direction are shown in Fig. 2. In Figs. 2(a) and 2(c), the data are fitted to the function  $y = -v_1x + v_2x^2 + v_3x^3$ , where  $v_1 = v_{yx} = 0.219$  and  $v_1 = v_{zx} = -0.073$  are the linear Poisson's ratio. Especially, the out-of-plane linear Poisson's ratio under uniaxial strain in the  $x$  direction is always negative for the entire considered strain range from  $-10\%$  to  $50\%$ . Figures 2(b) and 2(d) show the resulting strains in the  $x$  and  $z$  directions under uniaxial strain in the  $y$  direction, respectively. The data are fitted to the function  $y = -v_1x$  and  $y = -v_1x + v_2x^2 + v_3x^3$ , respectively, with  $v_1 = v_{xy} = 1.025$  and  $v_1 = v_{zy} = 0.058$ , respectively. We noticed that the structure of SiS is similar to those of monolayer black phosphorus and arsenic [32,34], and all of them possess a negative out-of-plane Poisson's ratio. However, the direction of the applied uniaxial strain is different for the out-of-plane NPR: it is the  $x$  direction for SiS, while it is the  $y$  direction for monolayer black phosphorus and arsenic.

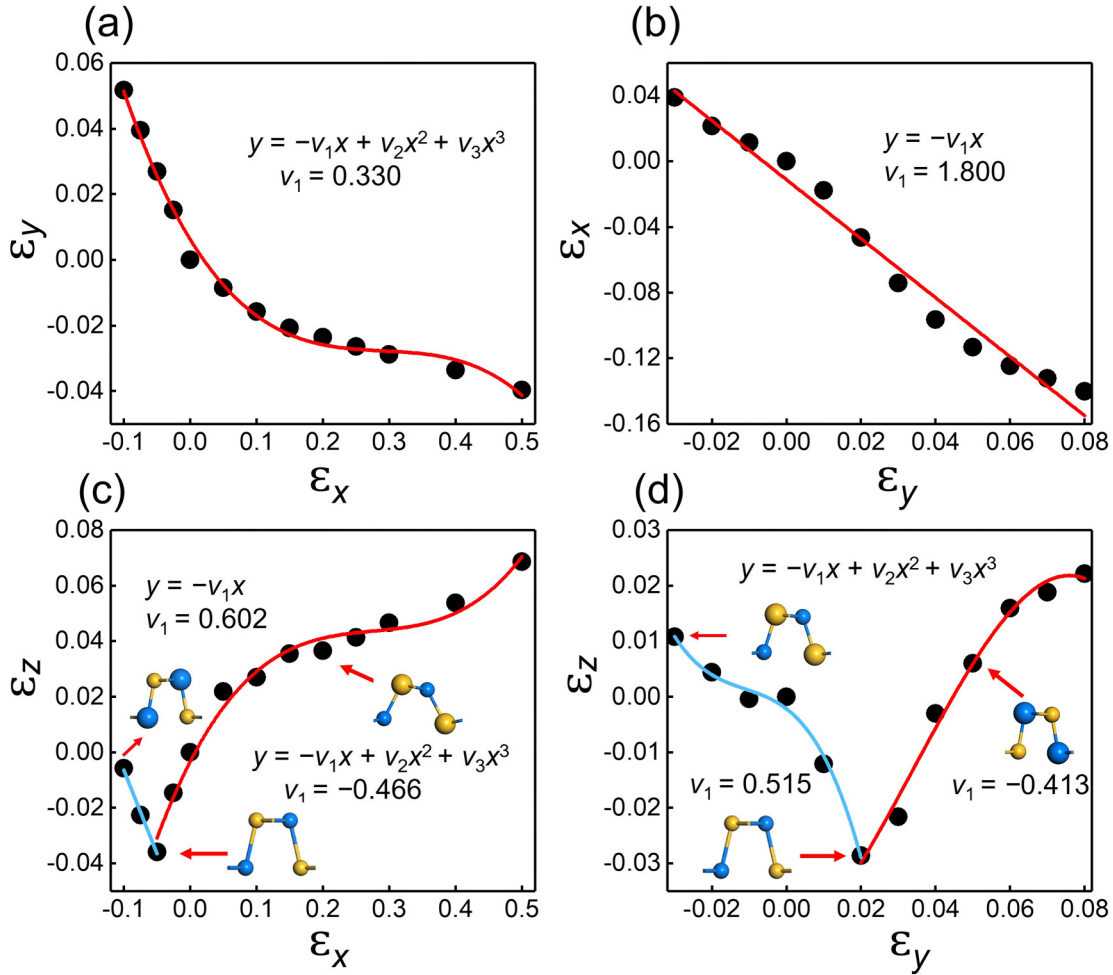


FIG. 3. Poisson's ratio as a function of uniaxial strain of monolayer SiSe in the  $x$  direction (a), (c), and  $y$  direction (b), (d). (a)  $\varepsilon_y$  versus  $\varepsilon_x$ . Data are fitted to function  $y = -\nu_1x + \nu_2x^2 + \nu_3x^3$ , with  $\nu_1 = 0.330$  as the linear Poisson's ratio. (b)  $\varepsilon_x$  versus  $\varepsilon_y$ . Data are fitted to function  $y = -\nu_1x$ , with  $\nu_1 = 1.800$  as the linear Poisson's ratio. (c)  $\varepsilon_z$  versus  $\varepsilon_x$ . Data are fitted to function  $y = -\nu_1x + \nu_2x^2 + \nu_3x^3$ , and  $y = -\nu_1x$ , with  $\nu_1 = -0.466$  and  $0.602$  as the linear Poisson's ratio, respectively. (d)  $\varepsilon_z$  versus  $\varepsilon_y$ . Data are fitted to function  $y = -\nu_1x + \nu_2x^2 + \nu_3x^3$ , with  $\nu_1 = 0.515$  and  $-0.413$  as the linear Poisson's ratio, respectively.

The Poisson's ratios of monolayer SiSe for uniaxial strain in the  $x$  direction and in the  $y$  direction are shown in Fig. 3. We first investigate the in-plane correspondence of monolayer SiSe under the strain. Figure 3(a) shows the strain in the  $y$  direction under uniaxial strain in the  $x$  direction. The data show a nonlinear behavior and can be fitted to the function  $y = -\nu_1x + \nu_2x^2 + \nu_3x^3$ . The parameter  $\nu_1 = \nu_{yx} = 0.330$  can be regarded as the linear Poisson's ratio. Figure 3(b) shows the strain in the  $x$  direction under uniaxial strain in the  $y$  direction. The data are fitted to the function  $y = -\nu_1x$ , where the linear Poisson's ratio is  $\nu_1 = \nu_{xy} = 1.800$ . Interestingly, monolayer SiSe has an in-plane positive Poisson's ratio  $\nu_{xy}$  approaching 2, and monolayer SiS and  $\alpha$ -antimony also have in-plane positive Poisson's ratio  $\nu_{xy}$  larger than 1. It means that the transverse response strain  $\varepsilon_x$  has a much larger magnitude than the applied longitudinal strain  $\varepsilon_y$ . This intrinsic property can be applied to strain amplifiers of functional nanodevices [62–64].

Next, we focus on the out-of-plane correspondence of monolayer SiSe under an in-plane uniaxial strain. The strain

in the  $z$  direction under uniaxial strain in the  $x$  direction is shown in Fig. 3(c). The atoms located at the outmost atomic layers under  $\varepsilon_x = 0$  are Si atoms from the side view. This Si-Se-Se-Si four-layer puckered binary structure remains under  $\varepsilon_x > -0.05$ . However, it changes into a double atomic layer structure with Si and Se atoms locating in the same plane under  $\varepsilon_x = -0.05$ . Further increasing the compression strength ( $\varepsilon_x < -0.05$ ) makes the Se atoms locate at the outmost plane (Se-Si-Si-Se structure). The buckling of the layer becomes more apparent under the compressible strain. A linear behavior is observed under  $\varepsilon_x < -0.05$  and the data are fitted to the function  $y = -\nu_1x$  with  $\nu_1 = \nu_{zx} = 0.602$ . A strong nonlinear behavior is observed under  $\varepsilon_x > -0.05$  and the data are fitted to the function  $y = -\nu_1x + \nu_2x^2 + \nu_3x^3$  with  $\nu_1 = \nu_{zx} = -0.466$ . It is interesting to notice that the Poisson's ratio of the 2D monoelemental monolayer black phosphorus and arsenic with the same puckered structure is not negative in this direction. The strain in the  $z$  direction under uniaxial strain in the  $y$  direction is shown in Fig. 3(d). As shown in the inset, the Si-Se-Se-Si four-layer puckered

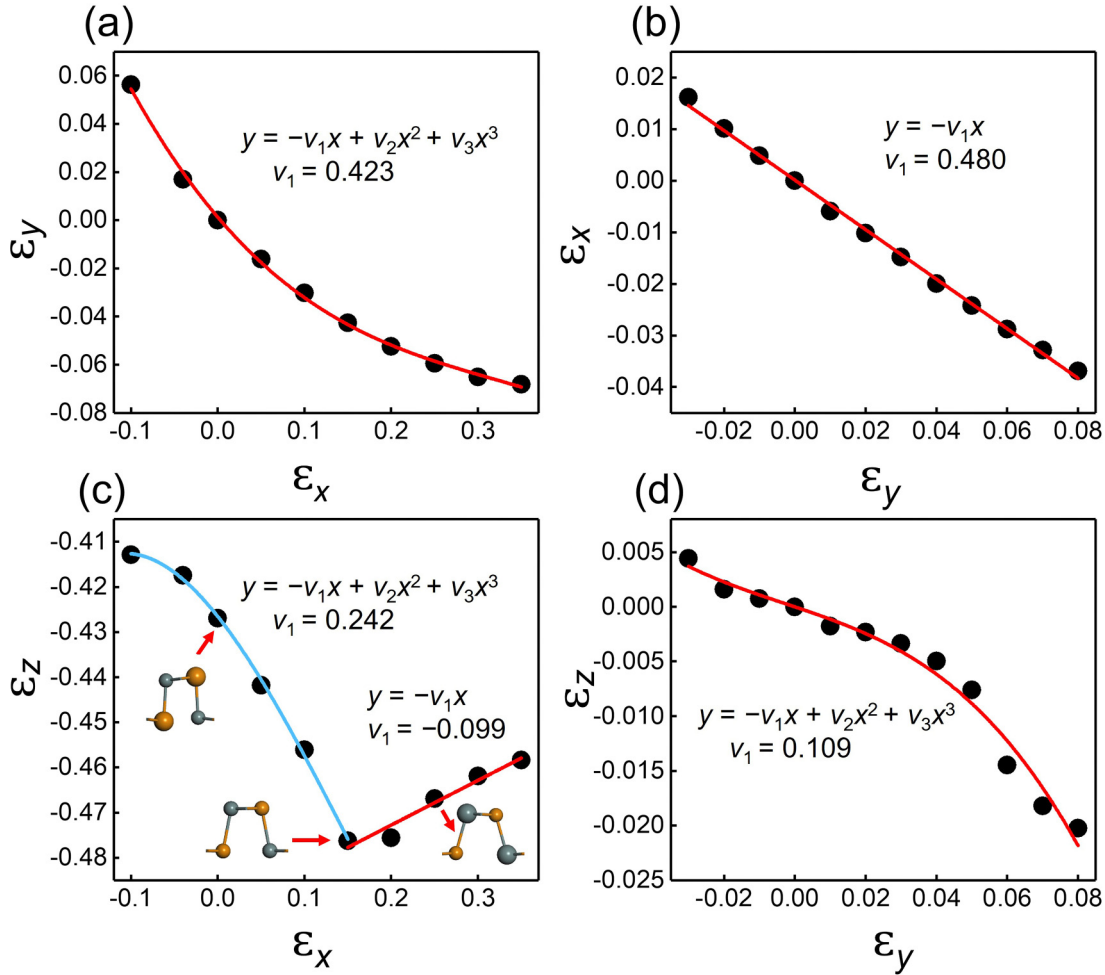


FIG. 4. Poisson's ratio as a function of uniaxial strain of monolayer SnTe in the  $x$  direction (a), (c), and  $y$  direction (b), (d). (a)  $\varepsilon_y$  versus  $\varepsilon_x$ . Data are fitted to function  $y = -v_1x + v_2x^2 + v_3x^3$ , with  $v_1 = 0.423$  as the linear Poisson's ratio. (b)  $\varepsilon_x$  versus  $\varepsilon_y$ . Data are fitted to function  $y = -v_1x$ , with  $v_1 = 0.480$  as the linear Poisson's ratio. (c)  $\varepsilon_z$  versus  $\varepsilon_x$ . Data are fitted to function  $y = -v_1x + v_2x^2 + v_3x^3$ , and  $y = -v_1x$ , with  $v_1 = 0.242$  and  $-0.099$  as the linear Poisson's ratio, respectively. (d)  $\varepsilon_z$  versus  $\varepsilon_y$ . Data are fitted to function  $y = -v_1x + v_2x^2 + v_3x^3$ , with  $v_1 = 0.109$  as the linear Poisson's ratio.

binary structure changes into Se-Si-Si-Se when  $\varepsilon_y = 0.02$ . Strong nonlinear behavior is observed, and the data are fitted to the function  $y = -v_1x + v_2x^2 + v_3x^3$ , where  $v_1 = v_{zy} = 0.515$  and  $-0.413$  for  $\varepsilon_y < 0.02$  and  $\varepsilon_y > 0.02$ , respectively. This NPR of monolayer SiSe ( $-0.413$ ) is about 15 and four times greater than its monolayer black phosphorus ( $-0.027$ ) [32] and arsenic ( $-0.093$ ) [34] counterparts, respectively.

For monolayer SnTe (Fig. 4), both the two in-plane Poisson's ratio  $\nu_{yx}$  (0.423) and  $\nu_{xy}$  (0.480) are positive like other puckered materials. However, the value of  $\nu_{xy}$  is noticeably small compared with other puckered materials (Table I). In Fig. 4(c), the out-of-plane Poisson's ratio  $\nu_{zx}$  is positive (0.242) when the outmost layer are the  $X$  atoms, while it becomes negative ( $-0.099$ ) when a structural transformation happens and the outmost atoms are  $M$  atoms. This is similar to the case of SiSe. In Fig. 4(d), the out-of-plane Poisson's ratio  $\nu_{zy}$  is positive (0.109).

The Poisson's ratios of monolayer W-Sb and aW-Sb are shown in Fig. 5 for uniaxial strain in the  $x$  and  $y$  directions. Similar to the cases of SiS and SiSe, W-Sb shows a small value of  $\nu_{yx}$  (0.301) and a large value of  $\nu_{xy}$  greater than 1 (1.375).

aW-Sb also shows a small value of  $\nu_{yx}$  (0.273), but its value of  $\nu_{xy}$  (0.689) is the smallest among those of the 2D puckered layers in Table I. Therefore, it is expected that applying a uniaxial strain along the  $y$  direction would have a relatively small effect in changing the lattice along the  $x$  direction

TABLE I. Poisson's ratio of monolayer puckered structures.

Materials	$\nu_{yx}$	$\nu_{xy}$	$\nu_{zx}$	$\nu_{zy}$
SiS	0.219	1.025	$-0.073$	0.058
SiSe	0.330	1.800	$0.602$ & $-0.466$	$0.515$ & $-0.413$
GeS [66]	0.420	1.401	$-0.208$	0.411
GeSe [66]	0.391	1.039	0.583	$-0.433$
SnS [66]	0.422	0.961	$-0.004$	0.404
SnSe [66]	0.423	0.851	$-0.210$	0.352
SnTe	0.423	0.480	$0.242$ & $-0.099$	0.109
BP [32]	0.400	0.930	0.046	$-0.027$
As [34]	0.350	1.070	0.130	$-0.093$
W-Sb	0.301	1.375	0.116	$-0.093$
aW-Sb	0.273	0.689	0.656	0.315

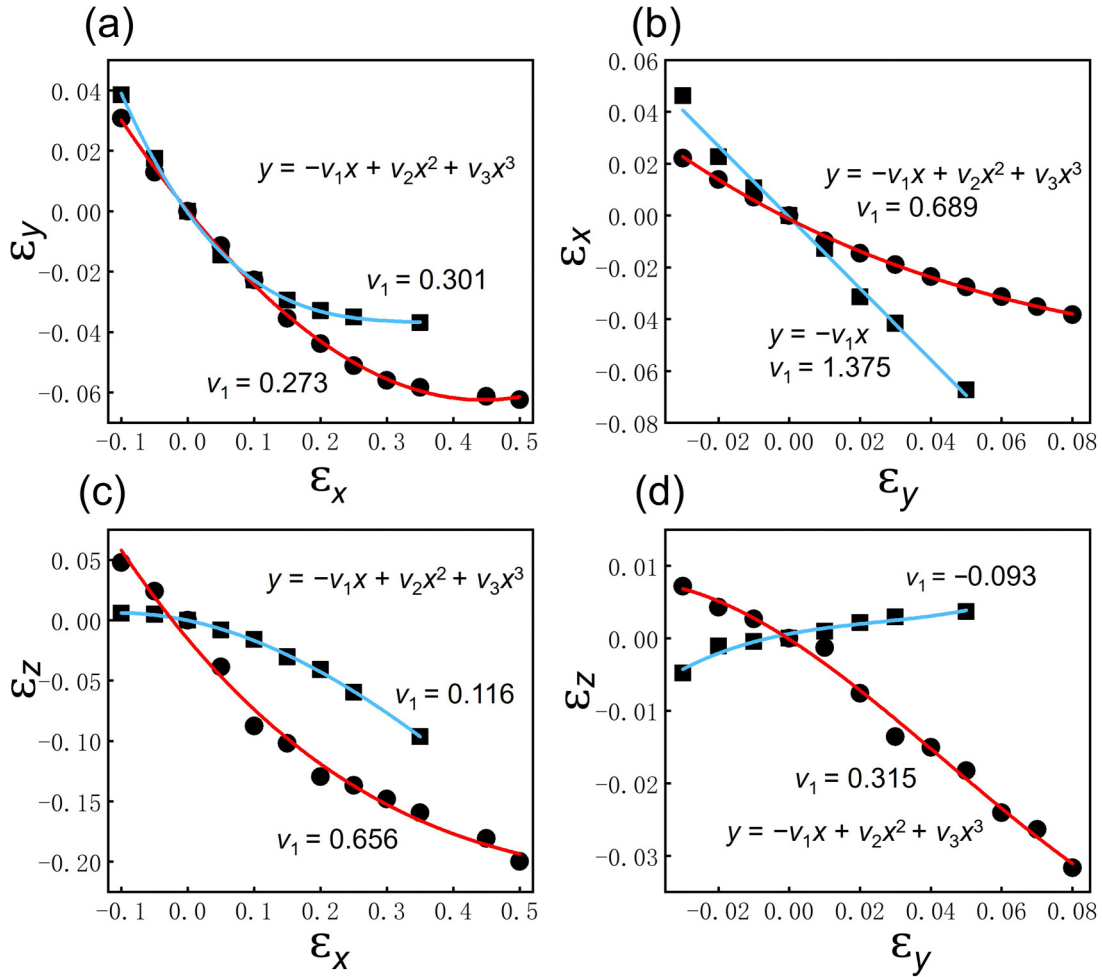


FIG. 5. Poisson's ratio as a function of uniaxial strain of monolayer W-phase and aW-phase antimonene in the  $x$  direction (a), (c), and  $y$  direction (b), (d). (a)  $\varepsilon_y$  versus  $\varepsilon_x$ . Data are fitted to function  $y = -v_1x + v_2x^2 + v_3x^3$ , with  $v_1 = 0.301$  and  $0.273$  as the linear Poisson's ratio. (b)  $\varepsilon_x$  versus  $\varepsilon_y$ . Data are fitted to function  $y = -v_1x + v_2x^2 + v_3x^3$ , with  $v_1 = 0.689$  and  $1.375$  as the linear Poisson's ratio. (c)  $\varepsilon_z$  versus  $\varepsilon_x$ . Data are fitted to function  $y = -v_1x + v_2x^2 + v_3x^3$ , with  $v_1 = 0.656$  and  $0.116$  as the linear Poisson's ratio. (d)  $\varepsilon_z$  versus  $\varepsilon_y$ . Data are fitted to function  $y = -v_1x + v_2x^2 + v_3x^3$ , with  $v_1 = 0.315$  and  $-0.093$  as the linear Poisson's ratio.

compared with other 2D puckered monolayers. As for the out-of-plane Poisson's ratio, monolayer W-Sb shows a positive value along the  $x$  direction ( $v_{zx} = 0.116$ ) and a negative one along the  $y$  direction ( $v_{zy} = -0.093$ ) like SiS. On the other hand, the out-of-plane Poisson's ratio of monolayer aW-Sb in both the  $x$  direction and  $y$  direction are positive ( $v_{zx} = 0.656$  and  $v_{zy} = 0.315$ ). In Table I, the in-plane and out-of-plane Poisson's ratio of the puckered monolayers are summarized. A detailed analysis regarding the relation between the Poisson's ratio and geometry changes is presented in the Supplemental Material (Figs. S2–S4).

Previous numerical simulations predict a positive PR of graphene under normal conditions [15–17] and the PR becomes negative at high temperatures [15], or in the presence of sufficiently strong disorder [18–20]. Recent theoretical work further demonstrates the dependence of PR of graphene on the applied stress [22,23]. It is interesting to check if a similar dependence exists in the puckered layers. Figure S5 shows the absolute PR and differential PR of monolayer SiS under different stress. With increasing stress, both the absolute and

differential in-plane PR ( $v_{yx}^{ab}$  and  $v_{yx}^{diff}$ ) show a decreasing trend, and both the absolute and differential out-of-plane PR ( $v_{zx}^{ab}$  and  $v_{zx}^{diff}$ ) show an increasing trend. While being close to low stress (0–0.5 GPa), the absolute and differential PR differ in the range of larger stress (>0.5 GPa or <0 GPa). With a stress in the range of  $-1$  to  $1$  GPa, the difference of the absolute PR and differential PR of monolayer SiS is up to  $0.1$  for the in-plane ones and  $0.05$  for the out-of-plane ones.

### C. Deformation mechanism

Although sharing the same puckered structures, the out-of-plane Poisson's ratio behaviors of monolayer group V-enes and group-IV monochalcogenide are quite different. Some puckered layers show a negative out-of-plane Poisson's ratio along the  $x$  direction, some show a negative out-of-plane Poisson's ratio along the  $y$  direction, and some show positive ones along both the  $x$  and  $y$  directions. This difference is closely related to the subtle difference of the structures and compositions. Monolayer BP, As, or W-Sb is composed of

a single element ( $M = X$ ), forming a double-layer puckered structure. Monolayer aW-Sb composed of Sb atoms ( $M = X$ ) forms a four-layer puckered structure. Monolayer group-IV monochalcogenide is composed of group-IV ( $M$ ) and chalcogen elements ( $X$ ), forming a four-layer puckered binary structure.

Generally, a uniaxial tension affects the thickness of the puckered monolayer *via* two routes. For example, the application of an  $x$ -direction tension not only directly induces a deformation in the  $x$  direction but also indirectly introduces a deformation in the  $y$  direction through the in-plane structural coupling. It is the deformation in both the  $x$  and  $y$  directions that contributes to the change of the layer thickness. The strength of the in-plane structural coupling can be found from the parameters  $\nu_{xy}$  and  $\nu_{yx}$ . The former represents the deformation in the  $x$  direction induced by a  $y$ -directed tension, while the latter represents the deformation in the  $y$  direction induced by an  $x$ -directed tension.

We first analyze the effects of the  $x$ - and  $y$ -directed deformations on the  $MX$  layer thickness ( $\Delta d_x$  and  $\Delta d_y$ ) in Figs. 6 and 7, and then discuss the overall effects on the thickness ( $\Delta d = \Delta d_x + \Delta d_y$ ) for each type of puckered structures in Fig. 8. We focus on the case of tensile deformation in Figs. 6 and 7, and the effect of compressive deformation on the thickness is the contrary. Atom 3 is chosen as the original point, and the movements of atoms relative to atom 3 are indicated. Atoms 1 (3) and 2 (4) are  $M$  and  $X$  atoms, respectively. Atom 1' is the replica of atom 1 in the nearby lattice.

### 1. Deformation in the $x$ direction

Figure 6(a) shows the detailed structural relaxation in the two consecutive steps for the double-layer puckered structure (monolayer black phosphorus, arsenic, and W-phase Sb). With a tensile deformation in the  $x$  direction, the two bond angles remain equivalent because of the chemical symmetry [32]. So in the first step, the bonds 2–3 and 4–1' rotate downward around the atoms 3 and 4, respectively, in order to keep  $\theta_M = \theta_X$ . This rotation leads to a decrease in the atomic layer thickness. In the second step, atoms 1 and 4 relax along the  $x$  direction, but it does not affect the thickness of the layer. Therefore, the tensile deformation in the  $x$  direction leads to the decrease of the thickness of the double-layer puckered structure ( $\Delta d_x < 0$ ).

Similar to the case in Fig. 6(a), the stretching in the  $x$  direction makes bonds 2–3 and 4–1' rotate downward around atom 3 in the four-layer puckered structure with  $M = X$  [Fig. 6(b)]. Such rotation leads to a downward movement of atom 1 (1') relative to atom 3, and the thickness reduces ( $\Delta d_x < 0$ ).

The structural relaxation for the four-layer puckered binary structure (group-IV monochalcogenide) under tensile deformation in the  $x$  direction is shown in Figs. 6(c) and 6(d). The rotation of bonds around the group-IV elements  $M$  is expected to be harder than that around the chalcogen elements  $X$  [65]. In other words, the change of  $\theta_M$  is expected to be smaller compared with  $\theta_X$  induced by the tensile deformation in the  $x$  direction [66]. As shown in Fig. S3, the slopes of  $\theta_X$  are 60.0–67.1° per unit strain in the SiS, SiSe, and SnTe layers, while the slopes of  $\theta_M$  are only 9.7–17.1° per unit strain under

the strain in the  $x$  direction. This is due to the fact that the valence shell electron pair repulsion (VSEPR) [67] around the group-IV  $M$  atoms are more apparent than the chalcogen  $X$  atoms. Figure S6 shows the total electron density of SiS, SiSe, and aW-Sb. Each Si and Sb atoms are surrounded by four  $sp^3$  orbitals, and each S and Se atoms are surrounded by four  $p$ -type orbitals. Among the four orbitals, one is occupied by two lone paired electrons, while three of the others are occupied by bonding electrons pairs. In the case of aW-Sb, the electron density around the neighboring two Sb atoms are quite similar. On the contrary, the lone paired electrons are more concentrated in one side of the  $M$  atoms but more uniformly distributed around the  $X$  atoms in the cases of SiS and SiSe, indicating a stronger VSEPR around  $M$  atoms.

Figure 6(c) describes the cases with the  $M$  atoms locating outmost. In the first step, atom 2 rotates downward around atom 3. In the second step, bond 3–4 rotates upward around atom 3 in order to keep the rigid bond angle of  $\theta_M$ . It is noted that it is an upward movement for atom 3 in the second step, unlike the case of Fig. 6(b), in which atom 3 moves downward. This difference is related to the more flexible bond angles of the chalcogen elements  $X$  in this case. The above discussion also applies to the case in Fig. 6(d). In the third step, atom 1 relaxes along the out-of-plane direction under the resultant repulsion force from atoms 2 and 4 due to the shortened bonds 1–2 and 4–1'. Therefore, the thickness of the  $M$ - $X$ - $X$ - $M$  four-layer puckered structure increases under the tensile deformation in the  $x$  direction, resulting in an increased thickness ( $\Delta d_x > 0$ ).

Figure 6(d) describes the cases with  $X$  atoms locating outmost. In the first step, atom 3 rotates downward around atom 3, and the thickness of the layer is decreased because  $X$  atoms are the outermost atoms. In the second step, in order to maintain the original value of  $\theta_M$ , bond 3–4 rotates upward around atom 3, and this rotation further decreases the thickness. In the third step, atom 1 relaxes along the out-of-plane direction under the resultant force from atoms 2 and 4. However, the movement of atom 1 in this step has no effect on the thickness. An overall effect of the three steps is a decrease of the thickness under the tensile deformation in the  $x$  direction. Therefore, the  $X$ - $M$ - $M$ - $X$  four-layer puckered structure exhibits a decrease of the thickness ( $\Delta d_x < 0$ ).

### 2. Deformation in the $y$ direction

As shown in Fig. 7, the effects of the tensile deformation in the  $y$  direction on the thickness can be classified into two types. The left view parallel to the  $y$ - $z$  plane is provided. Clearly, the thickness remains almost unchanged in the double-layer structure ( $\Delta d_y \approx 0$ ), while reduces significantly in the four-layer structure ( $\Delta d_y < 0$ ) under a tensile deformation in the  $y$  direction. Similarly, under a compressive deformation in the  $y$  direction, it is not difficult to expect a nearly unchanged ( $\Delta d_y \approx 0$ ) and an increased thickness ( $\Delta d_y > 0$ ) in the double- and four-atomic layer structures.

### 3. Overall effects on the thickness

A common feature of the studied puckered structures is that they all possess positive in-plane Poisson's ratio  $\nu_{xy}$  and  $\nu_{yx}$

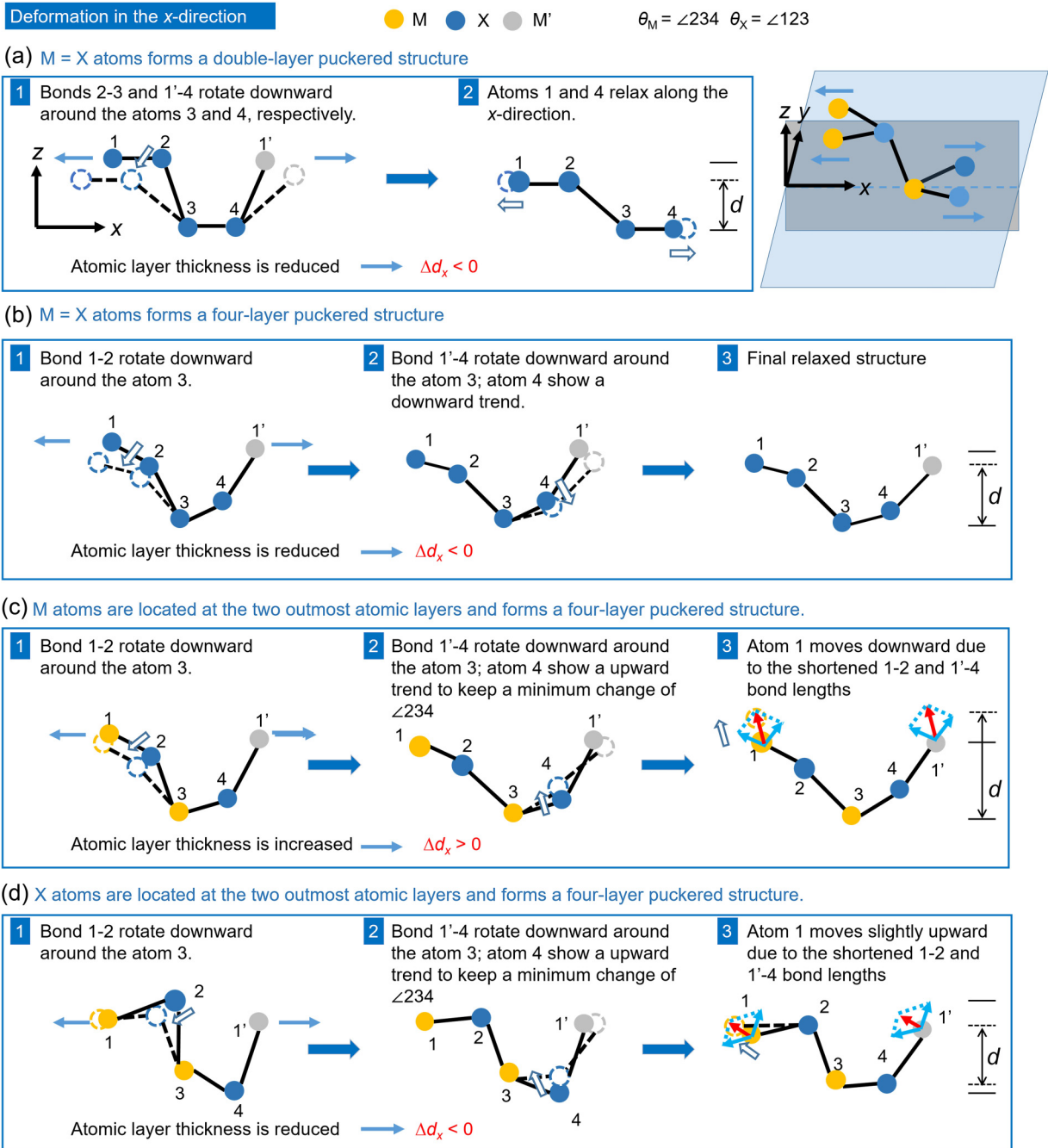


FIG. 6. Deformation mechanism upon uniaxial deformation in the x direction. The front view parallel to the XZ plane (grey area in the inset) of the MX structure is provided at each relaxation step. The solid and dashed M–X bonds indicate, respectively, the initial and final configurations at each step. The hollow blue arrows show the resulting movement of the M and X atoms. The red arrows show the resultant repulsion forces from atoms 2 and 4. The perspective of monolayer MX is next to (a).

[32,34,66]. Therefore, applying a uniaxial tension along the y direction on these structures induces a compression along the x direction. Similarly, applying a uniaxial tension along the x direction on these structures induces a compression along the y direction. The degree of compression depends on the value of  $\nu_{xy}$  and  $\nu_{yx}$ . Therefore, the total change of the thickness (and the out-of-plane Poisson's ratio) depends on both the changes induced by x- and y-directed deformation ( $\Delta d = \Delta d_x + \Delta d_y$ ), as summarized in Fig. 8.

(1) In type I with a double-layer structure (BP, As, and W-Sb;  $M = X$ ), the x-directed deformation plays a major role since the thickness changes induced by the y-directed deformation is neglectable.

(2) In type II with a four-layer structure (aW-Sb;  $M = X$ ), both the x- and y-directed deformation should be considered, and they render reverse trends of the thickness. Under a x-directed uniaxial tension, the x-directed deformation induced thickness reduction is expected to be more significant than the

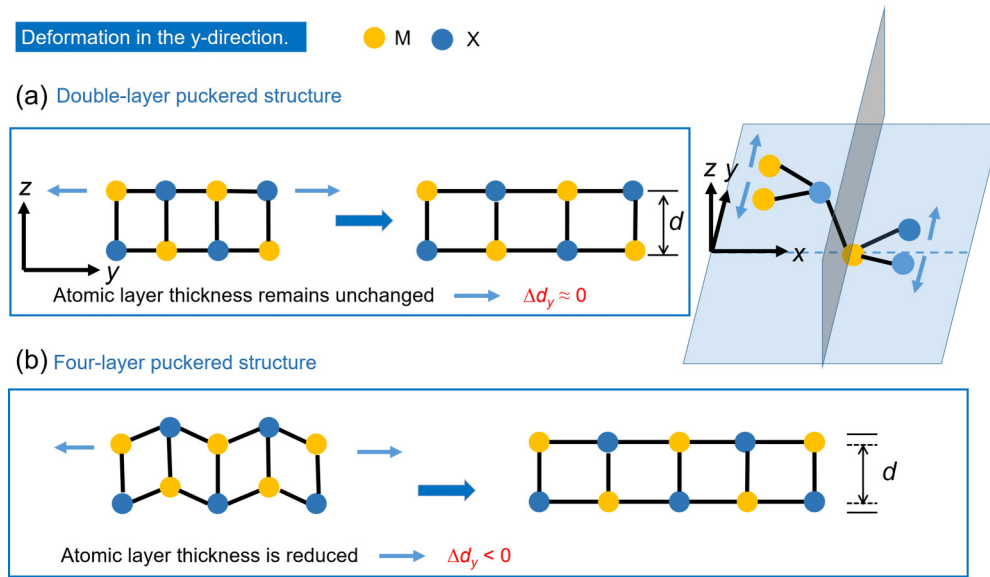


FIG. 7. Deformation mechanism under tensile deformation in the y direction. The left view parallel to the YZ plane of the MX structure is provided next to (a).

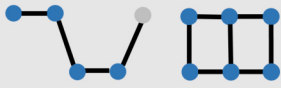
configuration	tension	thickness variation	Poisson's ratio
 BP, As, W-Sb	x-direction	$\Delta d_x < 0$ $\Delta d_y \approx 0$	$\Delta d < 0$ $\nu_{zx} > 0$
	y-direction	$\Delta d_x > 0$ $\Delta d_y \approx 0$	$\Delta d > 0$ $\nu_{zy} < 0$
 aW-Sb	x-direction	$\Delta d_x < 0$ $\Delta d_y > 0$	$\Delta d < 0$ $\nu_{zx} > 0$
	y-direction	$\Delta d_x > 0$ $\Delta d_y < 0$	$\Delta d < 0$ $\nu_{zy} > 0$
 SiS, SiSe*, SnS, SnSe, GeS, SnTe*	x-direction	$\Delta d_x > 0$ $\Delta d_y > 0$	$\Delta d > 0$ $\nu_{zx} < 0$
	y-direction	$\Delta d_x < 0$ $\Delta d_y < 0$	$\Delta d < 0$ $\nu_{zy} > 0$
 GeSe, SiSe*, SnTe*	x-direction	$\Delta d_x < 0$ $\Delta d_y > 0$	$\Delta d < 0$ $\nu_{zx} > 0$
	y-direction	$\Delta d_x > 0$ $\Delta d_y < 0$	$\Delta d > 0$ $\nu_{zy} < 0$
	y-direction	$\Delta d_x > 0$ $\Delta d_y < 0$	$\Delta d < 0$ $\nu_{zy} > 0$

FIG. 8. Classification of the out-of-plane Poisson's ratio in the pucker structure.  $\Delta d_x$  is the variation of the thickness due to the tensile deformation in the x direction.  $\Delta d_y$  is the variation of the thickness due to the tensile deformation in the y direction.  $\Delta d$  is the total variation ( $\Delta d = \Delta d_x + \Delta d_y$ ). The light yellow area indicates decreased layer thickness and positive out-of-plane Poisson's ratio. The light blue area indicates increased layer thickness and negative out-of-plane Poisson's ratio. The dominant variation between  $\Delta d_x$  and  $\Delta d_y$  is marked by the red font.

$y$ -directed deformation induced thickness increase, because of the relatively small value  $\nu_{yx}$  of 0.273. The resultant thickness reduces, and the corresponding Poisson's ratio  $\nu_{zx}$  is positive. Under a  $y$ -directed uniaxial tension, the thickness reduction induced by the  $y$ -directed deformation is more significant because this is a direct effect, and the out-of-plane Poisson's ratio  $\nu_{zy}$  is positive.

(3) Type III shows a four-layer structure with  $M$  atoms locating outmost ( $M \neq X$ ). The  $x$ -directed tension leads to a stretching in the  $x$  direction and a compression in the  $y$  direction, both resulting in a larger thickness. Thus, the Poisson's ratio  $\nu_{zx}$  is negative. Similarly, the  $y$ -directed tension leads to a stretching in the  $y$  direction and a compression in the  $x$  direction, both resulting in a smaller thickness. Thus, the Poisson's ratio  $\nu_{zy}$  is positive.

(4) Type IV shows a four-layer structure with  $X$  atoms locating outmost ( $M \neq X$ ). Unlike the case of type III, the deformation in the two directions results in reverse changes of the thickness. For GeSe and SiSe, no matter what tension is applied along the  $x$  or the  $y$  direction, the  $x$ -directed deformation is expected to play a major role in the thickness compared with the  $y$ -directed deformation, because of the small  $\nu_{yx}$  ( $< 0.5$ ) and large  $\nu_{xy}$  ( $> 1$ ). As a result, the thickness reduces under  $x$ -directed tension and increases under  $y$ -directed tension, and the corresponding Poisson's ratio  $\nu_{zx}$  and  $\nu_{zy}$  are positive and negative, respectively. For SnTe, the out-of-plane Poisson's ratio  $\nu_{zy}$  is positive. The sign difference of  $\nu_{zy}$  between SnTe and the other two members in type IV mainly stems from the different value of  $\nu_{xy}$ . Under strain along the  $y$  direction,  $\Delta d_x$  and  $\Delta d_y$  show reverse sign. When applying a tensile strain in the  $y$  direction, the direct deformation in the  $y$  direction leads to a thickness decrease ( $\Delta d_y < 0$ ) and the corresponding indirect deformation in the  $x$  direction leads to a thickness increase ( $\Delta d_x > 0$ ). Since the small  $\nu_{xy}$  in SnTe makes the latter effect less significant ( $|\Delta d_x| < |\Delta d_y|$ ), the overall thickness is expected to decrease upon the  $y$ -directed tensile strain ( $\Delta d < 0$ ), resulting in a positive  $\nu_{zx}$ . Conversely, in GeSe and SiSe, the thickness change due to the deformation in the  $x$  direction is more significant ( $|\Delta d_x| > |\Delta d_y|$ ) because of the large value of  $\nu_{xy}$  ( $> 1$ ) and thus the overall thickness increases upon  $y$ -directed tensile strain ( $\Delta d > 0$ ). It is noted that SiSe and SnTe have been classified into both types III

and IV, due to the occurrence of the structural transformation under strain.

#### IV. CONCLUSION

In summary, the geometric and mechanical properties of monolayer SiS, SiSe, SnTe, and orthorhombic antimonene are studied by first principles calculations. Monolayer SiS, SiSe, SnTe, and W-Sb possess negative out-of-plane Poisson's ratio, while aW-Sb does not. Especially, monolayer SiSe has large NPR under uniaxial strain in both the  $x$  direction ( $\nu_{zx} = -0.466$ ) and  $y$  direction ( $\nu_{zy} = -0.413$ ), which are 15 times that of monolayer black phosphorus ( $\nu_{zy} = -0.027$ ). This large Poisson's ratio is expected to improve the sensitivity of microsensor and protective performance of defense equipment. Moreover, the structural phase of monolayer SiSe and SnTe and their signs of the Poisson's ratio can be tuned by changing the strength and direction of the applied strain. In the end, a universal deformation mechanism of the intrinsic NPR for puckered structures (including monolayer BP, As, Sb, SiS, SiSe, GeS, GeSe, SnS, SnSe, and SnTe) is provided. Our mechanism reveals: (1) A 2D material with a black-phosphorous-like puckered structure does not guarantee an out-of-plane NPR; (2) The application of a uniaxial strain leads to the deformations of the lattice constant in both the  $x$  and  $y$  directions, and both deformations affect the thickness and thus the out-of-plane Poisson's ratio; (3) The type of the outmost atoms and the degree of the in-plane structural coupling determine the direction ( $x$  or  $y$ ) of the applied uniaxial strain that renders an out-of-plane NPR. Our work sheds light on the mechanical properties of the 2D materials with the puckered structures.

#### ACKNOWLEDGMENTS

This work was supported by the National Natural Science Foundation of China (Grants No. 11604019 and No. 61574020), the Fund of the State Key Laboratory of Information Photonics and Optical Communications (Beijing University of Posts and Telecommunications), and the Research Innovation Fund for College Students of Beijing University of Posts and Telecommunications.

- 
- [1] K. E. Evans, M. A. Nkansah, I. J. Hutchinson, and S. C. Rogers, *Nature (London)* **353**, 124 (1991).
  - [2] J. B. Choi and R. S. Lakes, *J. Mater. Sci.* **27**, 5375 (1992).
  - [3] R. S. Lakes and K. Elms, *J. Compos. Mater.* **27**, 1193 (1993).
  - [4] J. B. Choi and R. S. Lakes, *Int. J. Fract.* **80**, 73 (1996).
  - [5] F. Scarpa, *IEEE. Signal. Process. Mag.* **25**, 128 (2008).
  - [6] M. S. Avellaneda and Pieter J. Swart, *J. Acoust. Soc. Am.* **103**, 1449 (1998).
  - [7] M. Sanami, N. Ravirala, K. Alderson, and A. Alderson, *Proc. Eng.* **72**, 453 (2014).
  - [8] R. Lakes, *Science* **235**, 1038 (1987).
  - [9] R. Lakes, *J. Mater. Sci.* **26**, 2287 (1991).
  - [10] F. Milstein and K. Huang, *Phys. Rev. B* **19**, 2030 (1979).
  - [11] R. H. Baughman, J. M. Shacklette, A. A. Zakhidov, and S. Stafström, *Nature (London)* **392**, 362 (1998).
  - [12] A. Yeganeh-Haeri, D. J. Weidner, and J. B. Parise, *Science* **257**, 650 (1992).
  - [13] H. Ogi, M. Fukunaga, M. Hirao, and H. Ledbetter, *Phys. Rev. B* **69**, 024104 (2004).
  - [14] J. W. Jiang, T. Chang, X. Guo, and H. S. Park, *Nano Lett.* **16**, 5286 (2016).
  - [15] K. V. Zakharchenko, M. I. Katsnelson, and A. Fasolino, *Phys. Rev. Lett.* **102**, 046808 (2009).
  - [16] J. H. Los, A. Fasolino, and M. I. Katsnelson, *Phys. Rev. Lett.* **116**, 015901 (2016).
  - [17] G. Gui, J. Li, and J. Zhong, *Phys. Rev. B* **78**, 075435 (2008).
  - [18] J. N. Grima, S. Winczewski, L. Mizzi, M. C. Grech, R. Cauchi, R. Gatt, D. Attard, K. W. Wojciechowski, and J. Rybicki, *Adv. Mater.* **27**, 1455 (2015).

- [19] H. Qin, Y. Sun, J. Z. Liu, M. Li, and Y. Liu, *Nanoscale* **9**, 4135 (2017).
- [20] J. Wan, J.-W. Jiang, and H. S. Park, *Nanoscale* **9**, 4007 (2017).
- [21] P. Le Doussal and L. Radzihovsky, *Phys. Rev. Lett.* **69**, 1209 (1992).
- [22] Z. W. Ulissi, A. Govind Rajan, and M. S. Strano, *ACS Nano* **10**, 7542 (2016).
- [23] I. S. Burmistrov, I. V. Gornyi, V. Y. Kachorovskii, M. I. Katsnelson, J. H. Los, and A. D. Mirlin, *Phys. Rev. B* **97**, 125402 (2018).
- [24] Z. Gao, X. Dong, N. Li, and J. Ren, *Nano Lett.* **17**, 772 (2017).
- [25] S. Zhang, J. Zhou, Q. Wang, X. Chen, Y. Kawazoe, and P. Jena, *Proc. Natl. Acad. Sci. USA* **112**, 2372 (2015).
- [26] H. Sun, S. Mukherjee, and C. V. Singh, *Phys. Chem. Chem. Phys.* **18**, 26736 (2016).
- [27] Y. Wang, F. Li, Y. Li, and Z. Chen, *Nat. Commun.* **7**, 11488 (2016).
- [28] V. O. Özçelik, S. Cahangirov, and S. Ciraci, *Phys. Rev. Lett.* **112**, 246803 (2014).
- [29] L. Yu, Q. Yan, and A. Ruzsinszky, *Nat. Commun.* **8**, 15224 (2017).
- [30] R. Quhe, Q. Li, Q. Zhang, Y. Wang, H. Zhang, J. Li, X. Zhang, D. Chen, K. Liu, Y. Ye, L. Dai, F. Pan, M. Lei, and J. Lu, *Phys. Rev. Appl.* **10**, 024022 (2018).
- [31] H. Liu, A. T. Neal, Z. Zhu, Z. Luo, X. Xu, D. Tománek, and P. D. Ye, *ACS Nano* **8**, 4033 (2014).
- [32] J.-W. Jiang and H. S. Park, *Nat. Commun.* **5**, 4727 (2014).
- [33] Y. Du, J. Maassen, W. Wu, Z. Luo, X. Xu, and P. D. Ye, *Nano Lett.* **16**, 6701 (2016).
- [34] J. Han, J. Xie, Z. Zhang, D. Yang, M. Si, and D. Xue, *Appl. Phys. Express* **8**, 041801 (2015).
- [35] L. C. Gomes, A. Carvalho, and A. H. Castro Neto, *Phys. Rev. B* **92**, 214103 (2015).
- [36] R. Peng, Y. Ma, Z. He, B. Huang, L. Kou, and Y. Dai, *Nano Lett.* **19**, 1227 (2019).
- [37] P. E. Blöchl, *Phys. Rev. B* **50**, 17953 (1994).
- [38] G. Kresse and J. Furthmüller, *Comput. Mater. Sci.* **6**, 15 (1996).
- [39] J. P. Perdew, K. Burke, and M. Ernzerhof, *Phys. Rev. Lett.* **77**, 3865 (1996).
- [40] C. Kamal, A. Chakrabarti, and M. Ezawa, *Phys. Rev. B* **93**, 125428 (2016).
- [41] Y. Mao, J. Ben, J. Yuan, and J. Zhong, *Chem. Phys. Lett.* **705**, 12 (2018).
- [42] Z. Zhu, J. Guan, D. Liu, and D. Tománek, *ACS Nano* **9**, 8284 (2015).
- [43] D. Rocca, A. Abboud, G. Vaitheeswaran, and S. Lebegue, *Beilstein J. Nanotechnol.* **8**, 1338 (2017).
- [44] C. Chowdhury, S. Karmakar, and A. Datta, *J. Phys. Chem. C* **121**, 7615 (2017).
- [45] K. Chang, J. Liu, H. Lin, N. Wang, K. Zhao, A. Zhang, F. Jin, Y. Zhong, X. Hu, W. Duan, Q. Zhang, L. Fu, Q.-K. Xue, X. Chen, and S.-H. Ji, *Science* **353**, 274 (2016).
- [46] K. Chang, T. P. Kaloni, H. Lin, A. Bedoya-Pinto, A. K. Pandeya, I. Kostanovskiy, K. Zhao, Y. Zhong, X. Hu, Q.-K. Xue, X. Chen, S.-H. Ji, S. Barraza-Lopez, and S. S. P. Parkin, *Adv. Mater.* **31**, 1804428 (2019).
- [47] B. R. Tuttle, S. M. Alhassan, and S. T. Pantelides, *Phys. Rev. B* **92**, 235405 (2015).
- [48] J.-H. Yang, Y. Zhang, W.-J. Yin, X. G. Gong, B. I. Yakobson, and S.-H. Wei, *Nano Lett.* **16**, 1110 (2016).
- [49] S. Karmakar, C. Chowdhury, and A. Datta, *J. Phys. Chem. C* **120**, 14522 (2016).
- [50] M. Mehboudi, A. M. Dorio, W. Zhu, A. van der Zande, H. O. H. Churchill, A. A. Pacheco-Sanjuan, E. O. Harriss, P. Kumar, and S. Barraza-Lopez, *Nano Lett.* **16**, 1704 (2016).
- [51] M. Mehboudi, B. M. Fregoso, Y. Yang, W. Zhu, A. van der Zande, J. Ferrer, L. Bellaïche, P. Kumar, and S. Barraza-Lopez, *Phys. Rev. Lett.* **117**, 246802 (2016).
- [52] S. Barraza-Lopez, T. P. Kaloni, S. P. Poudel, and P. Kumar, *Phys. Rev. B* **97**, 024110 (2018).
- [53] J. Liu and S. T. Pantelides, *Phys. Rev. Lett.* **120**, 207602 (2018).
- [54] J. Liu and S. T. Pantelides, *Appl. Phys. Express* **11**, 101301 (2018).
- [55] See Supplemental Material at <http://link.aps.org/supplemental/10.1103/PhysRevMaterials.3.054002> for structural properties, relation between Poisson's ratio and structural changes, Poisson's ratio under stress, and total electron density.
- [56] S. Zhang, S. Guo, Z. Chen, Y. Wang, H. Gao, J. Gómez-Herrero, P. Ares, F. Zamora, Z. Zhu, and H. Zeng, *Chem. Soc. Rev.* **47**, 982 (2018).
- [57] G. Wang, R. Pandey, and S. P. Karna, *ACS Appl. Mater. Interfaces* **7**, 11490 (2015).
- [58] Z.-Q. Shi, H. Li, Q.-Q. Yuan, Y.-H. Song, Y.-Y. Lv, W. Shi, Z.-Y. Jia, L. Gao, Y.-B. Chen, W. Zhu, and S.-C. Li, *Adv. Mater.* **31**, 1806130 (2018).
- [59] T. Märkl, P. J. Kowalczyk, M. Le Ster, I. V. Mahajan, H. Pirie, Z. Ahmed, G. Bian, X. Wang, T. C. Chiang, and S. A. Brown, *2D Mater.* **5**, 011002 (2017).
- [60] O. Ü. Aktürk, V. O. Özçelik, and S. Ciraci, *Phys. Rev. B* **91**, 235446 (2015).
- [61] Y. Xu, B. Peng, H. Zhang, H. Shao, R. Zhang, and H. Zhu, *Ann. Phys. (Berlin)* **529**, 1600152 (2017).
- [62] X. Yu, H. Cheng, M. Zhang, Y. Zhao, L. Qu, and G. Shi, *Nat. Rev. Mater.* **2**, 17046 (2017).
- [63] Z. Chang, J. Deng, G. G. Chandrakumara, W. Yan, and J. Z. Liu, *Nat. Commun.* **7**, 11972 (2016).
- [64] Y. Huang, J. Liang, and Y. Chen, *J. Mater. Chem.* **22**, 3671 (2012).
- [65] C. Kittel, *Introduction to Solid State Physics* (Wiley, New York, 1986).
- [66] X. Kong, J. Deng, L. Li, Y. Liu, X. Ding, J. Sun, and J. Z. Liu, *Phys. Rev. B* **98**, 184104 (2018).
- [67] R. J. Gillespie, *Coord. Chem. Rev.* **252**, 1315 (2008).